JACS
JOURNAL OF THE AMERICAN CHEMICAL SOCIETY
pubs.acs.org/JACS

Article

Mining the Carbon Intermediates in Plastic Waste Upcycling for Constructing C−S Bond

Hongxing Kang, Dong He, Christopher Turchiano, Xingxu Yan, Jingtong Chai, Melanie Weed, Gregory I. Elliott, David Onofrei, Xiaoqing Pan, Xiangheng Xiao, and Jing Gu*

Cite This: J. Am. Chem. Soc. 2024, 146, 18639−18649

Read Online

ACCESS | Metrics & More | Article Recommendations | Supporting Information

ABSTRACT: Postconsumer plastics are generally perceived as valueless with only a small portion of plastic waste being closed-loop recycled into similar products while most of them are discarded in landfills. Depositing plastic waste in landfills not only harms the environment but also signifies a substantial economic loss. Alternatively, constructing value-added chemical feedstocks via mining the waste-derived intermediate species as a carbon (C) source under mild electrochemical conditions is a sustainable strategy to realize the circular economy. This proof-of-concept work provides an attractive "turning trash to treasure" strategy by integrating electrocatalytic polyethylene terephthalate (PET) plastic upcycling with a chemical C−S coupling reaction to synthesize organosulfur compounds, hydroxymethanesulfonate (HMS). HMS can be produced efficiently (Faradaic efficiency, FE of ∼70%) via deliberately capturing electrophilic intermediates generated in the PET monomer (ethylene glycol, EG) upcycling process, followed by coupling them with nucleophilic sulfur (S) species (i.e., SO_3^{2-} and HSO_3^-). Unlike many previous studies conducted under alkaline conditions, PET upcycling was performed over an amorphous MnO_2 catalyst under near-neutral conditions, allowing for the stabilization of electrophilic intermediates. The compatibility of this strategy was further investigated by employing biomass-derived compounds as substrates. Moreover, comparable HMS yields can be achieved with real-world PET plastics, showing its enormous potential in practical application. Lastly, Density function theory (DFT) calculation reveals that the C−C cleavage step of EG is the rate-determining step (RDS), and amorphous MnO_2 significantly decreases the energy barriers for both RDS and C−S coupling when compared to the crystalline counterpart.

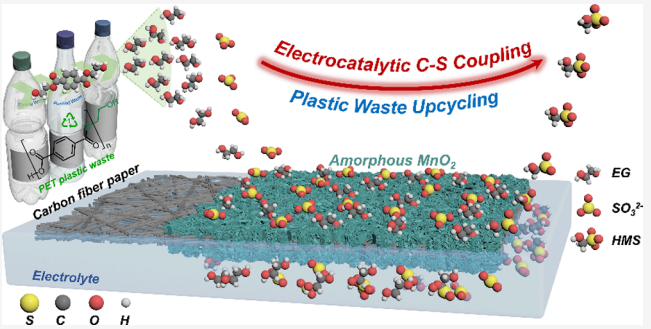

INTRODUCTION

Plastics, being chemically stable, structurally customizable, and easily transportable, have become a remarkable category of materials that revolutionized human lives over the past 150 years.[1,2] The amount of plastics being used is increasing exponentially, with a projection that 25 billion tons of plastic waste will be generated by 2050.[3] Most of the plastic waste ends up being put into our earth's crust, with just 2% of plastic waste being recycled via conventional mechanical recycling methods.[4] It is important to note that the vast majority of plastics (∼70%) are synthesized from a petroleum-derived chemical process.[2] Thus, postconsumer plastics are essential "trapped" hydrocarbon fossil fuels that have been drilled, purified, processed, and used only briefly. Therefore, harvesting carbon and energy resources from these plastic waste streams will put the untapped carbon resources back into their economic cycle.

Transforming plastic waste into value-added chemicals through electrocatalysis is a promising and green approach to mitigate environmental issues raised by postconsumer plastics. Polyethylene terephthalate (PET), commonly found in packaging and textiles with an annual production of over 70 million tons, is utilized here as a model plastic waste.[5] Prior to electrocatalytic upcycling, PET usually undergoes a base-catalyzed hydrolysis reaction to produce ethylene glycol (EG) and terephthalate (TPA) monomers (Figure 1a). Subsequently, the hydrolysate is utilized directly for electrolysis. During this process, EG is oxidized at the anode, whereas the TPA remains unchanged. Protons at the cathode are transformed into green hydrogen gas. Compared to conventional water electrolysis, replacing anodic oxygen evolution reaction (OER) with PET upcycling will not only solve environmental concerns caused by plastic waste but also enable the retrieval of chemical energy stored within plastic waste.

Inspired by recent developments in CO_2 conversion, carbon−heteroatom (C−X, X = N, S) bond formation can proceed by

Received: April 22, 2024
Revised: June 7, 2024
Accepted: June 10, 2024
Published: June 25, 2024

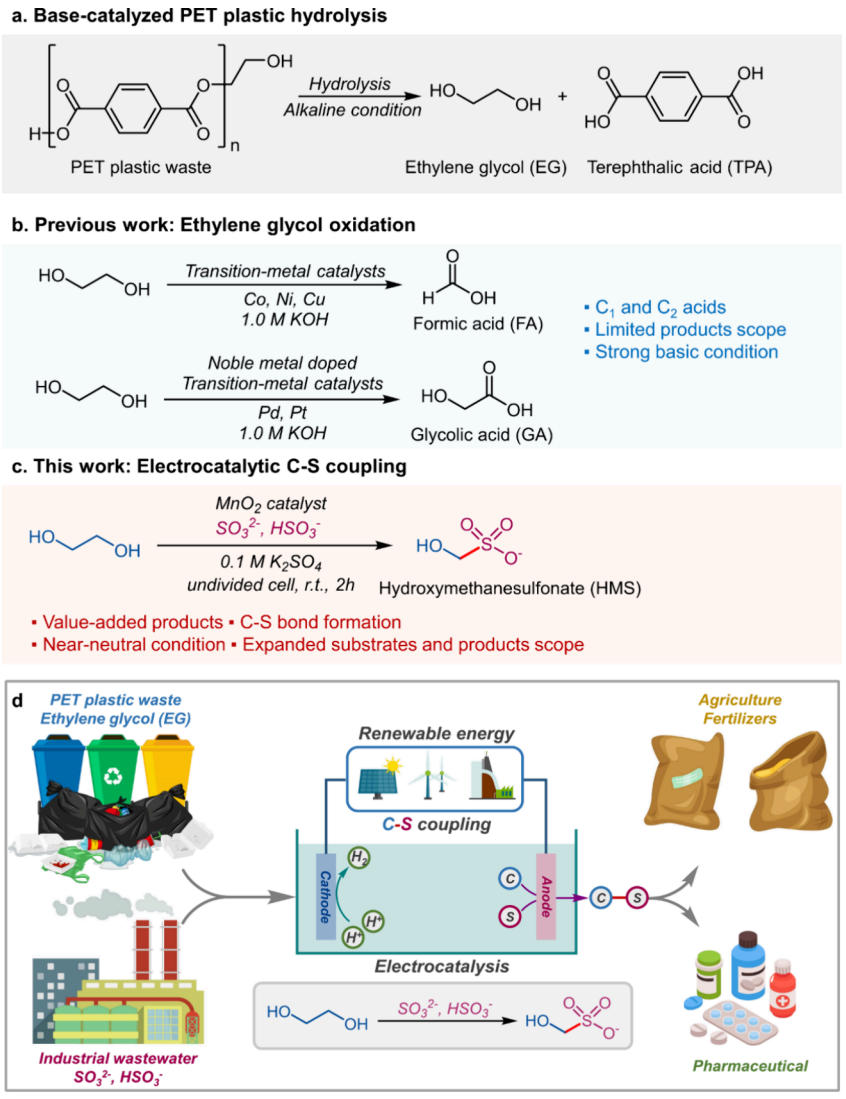

Figure 1. (a) Base-catalyzed PET plastic hydrolysis reaction to produce EG and TPA. (b) Previous work on EG electrooxidation for C_1 and C_2 products formation under alkaline conditions. (c) This work: Electrocatalytic C−S coupling reaction by capturing electrophile intermediates in EGOR and coupling them with sulfur oxides under near-neutral conditions. (d) Coupling electrocatalytic upcycling of PET plastic wastes with sulfur oxides derived from industrial wastewater for an all-encompassing "waste to value" strategy.

capturing the active electrophilic intermediate species (i.e., *CH_2OH, *CHOH, *COH) and then chemically reacting them with nucleophiles containing N or S.[6−9] Electrocatalytic C−N formation has been explored extensively in CO_2 reduction.[6,7] For instance, Saravanakumar et al. showed a TiO_2−Nafion nanocomposite electrode can achieve a 40% Faradaic efficiency (FE) for urea production by simultaneously reducing CO_2 and NO_3^-.[8] Later, Wang and co-workers demonstrated methylamine can be synthesized through the coreduction of CO_2 and NO_3^- (with an optimal 13% FE), enabled by cobalt phthalocyanine molecules supported on carbon nanotubes (CoPc/CNT).[10] Recently, the scope of C−X formation has been expanded by Kornienko et al. via coupling the *CHOH intermediate generated in CO_2 reduction with nucleophilic SO_3^{2-} on a copper (Cu)-based catalyst to form sulfonates. Sulfonates are important chemical feedstocks that have diverse applications in organic synthesis, lubricants, and textile industry.[11−16] Unfortunately, due to the poor selectivity of the Cu catalyst to stabilize the intermediates, the FEs for the sulfonates only range from 4.7% to 9.5%.[9] At the same time, we noticed that similar electrophilic intermediates, like formaldehyde (*CH_2O), are well-recognized intermediates in EG oxidation reaction (EGOR). Formaldehyde, being a reactive electrophile, can be attacked by various nucleophiles (like NH_3 and SO_3^{2-}), which provides a rational pathway to construct C−X bonds.

Sulfur is the fifth most abundant element on Earth and organosulfur compounds have a wide application in organic synthesis, pharmaceuticals, and advanced materials.[17−21] However, traditional organic C−S formation methods suffer from complex synthetic procedures, the utilization of toxic precursors and solvents, and the generation of toxic byproducts, limiting their sustainable large-scale applications.[22−25] Renewable energy-driven strategies, such as electrochemical and photochemical routes, have been explored. For example, carbon nitride can act as a charge storage material and radical anion for direct C−H thiolation using elemental S as the S source under visible light irradiation.[26] In addition, Pan and co-workers demonstrated the oxysulfenylation of styrene derivatives can be achieved under mild electrochemical conditions by selectively

https://doi.org/10.1021/jacs.4c05512
J. Am. Chem. Soc. 2024, 146, 18639−18649

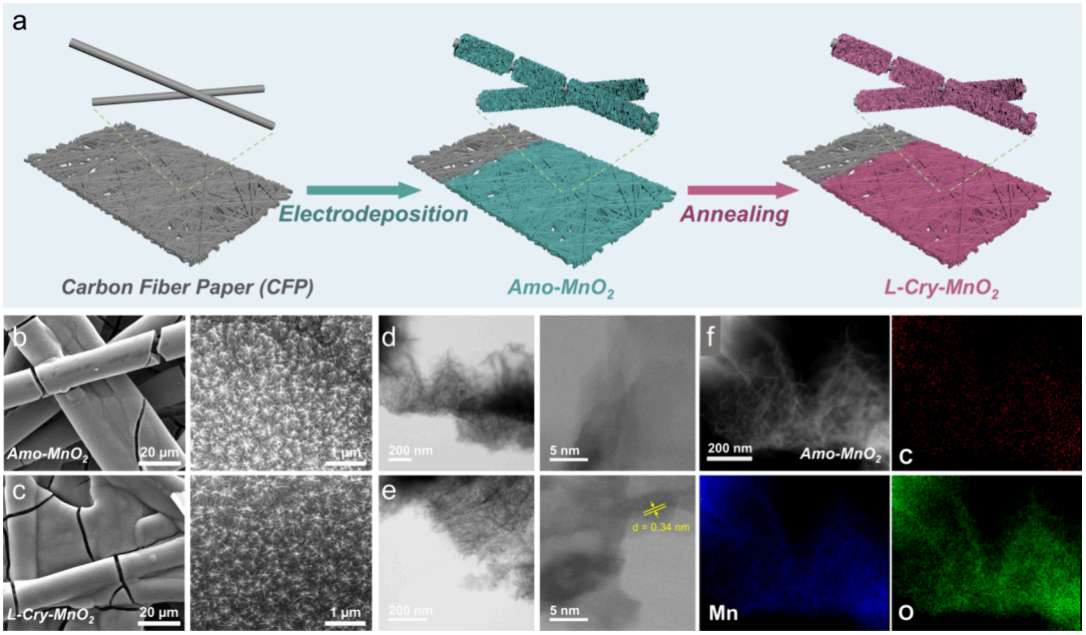

Figure 2. (a) Synthesis scheme of Amo-MnO_2 and L-Cry-MnO_2 on CFP. Although the structures of manganese oxides are complicated, nonstoichiometric oxides often contain additional metal cations, physisorbed water, and structural vacancies. In this work, we simply denote these materials as "MnO_2". SEM images of (b) Amo-MnO_2 and (c) L-Cry-MnO_2 with different magnitudes. Bright-field STEM images of (d) Amo-MnO_2 and (e) L-Cry-MnO_2 with different magnitudes. (f) A high-angle annular dark-field STEM image of Amo-MnO_2 and the corresponding C, Mn, O elemental mappings.

oxidizing thiols/thiophenols into sulfur radicals.[27] Despite these great achievements, the direct coupling of C−S utilizing plastic wastes and sulfur oxides (SO_3^{2-}, HSO_3^-) in an aqueous solution at room temperature has yet to be accomplished.

One fundamental challenge to accomplish the aforementioned C−S coupling reaction is the instability of the formaldehyde intermediates under strongly alkaline conditions. Under alkaline conditions, formaldehyde could be rapidly oxidized to formate or undergo a Cannizzaro reaction,[28] disproportionating into formate and methanol. Unfortunately, many of the electrocatalysts created for PET upcycling work best in alkaline environments. For instance, transition metals, such as Ni-,[29] Co-,[30] and Cu[31]-based catalysts, achieved high selectivity for converting EG monomer into C_1 products, such as formate. In these studies, EG was initially oxidized to glycolaldehyde, then oxidized to either glycolic acid or glyoxal, and underwent C−C bond cleavage to produce formate.[32,33] On the other side, noble metal doped electrocatalysts, such as Pd/Ni$(OH)_2$[34] and Pt/γ-NiOOH/NF,[35] show a great potential to oxidize EG to C_2 products, such as glycolate, under alkaline conditions (Figure 1b). To stabilize the formaldehyde intermediate, it is necessary to identify an electrocatalyst capable of oxidizing EG under near-neutral (or acidic) conditions. Nevertheless, most transition metal-based electrocatalysts such as oxides, hydroxides, and oxyhydroxides suffer from stability issues under near-neutral (or acidic) conditions.[36,37] Fortunately, MnO_2 has recently gained recognition as a superior catalyst with long-lasting stability for alcohol oxidation in acidic environments.[38]

Inspired by these pioneering works, we developed a plastic waste upcycling strategy via coupling electrocatalytic PET plastic waste conversion with C−S bond formation to synthesize hydroxymethanesulfonate (HMS) over an amorphous MnO_2 (Amo-MnO_2) (Figure 1c). When Amo-MnO_2 was employed, up to ∼55% FE of EG to formate conversion could be achieved. In addition, HMS was efficiently synthesized with a superior FE (up to ∼70%) when EGOR was integrated with C−S coupling. Subsequently, real-world plastic wastes were applied as substrates for HMS synthesis. Crude TPA could be first recovered from commercial PET plastic wastes via hydrolysis, acidification, and separation. Further, an impressive selectivity (∼65% FE) for HMS production can be accomplished within just 2 h electrolysis of PET hydrolysate with the presence of sulfoxides (SO_3^{2-} and HSO_3^-). It is worth noting that SO_3^{2-} and HSO_3^- are common species in industrial wastewater. Therefore, this approach not only aids in upcycling plastic wastes but also contributes to wastewater treatment, ultimately forming an all-encompassing "waste to value" strategy (Figure 1d).

RESULTS AND DISCUSSION

Catalyst Characterization. The amorphous MnO_2 (Amo-MnO_2) electrocatalyst was synthesized on carbon fiber paper (CFP) via electrodeposition (see Supporting Information (SI) for more information) (Figure S1). As a control, a low-crystalline MnO_2 (L-Cry-MnO_2) was synthesized by annealing Amo-MnO_2 at 300 °C (Figure 2a). Amo-MnO_2 reveals a uniform and dense coverage of MnO_2 nanosheet by scanning electron microscopy (SEM) and scanning transmission electron microscopy (STEM) (Figure 2b, 2d, and Figures S2, S3). After annealing, L-Cry-MnO_2 displays a similar nanosheet morphology to that of Amo-MnO_2, indicating that the annealing process plays a minor role in altering the morphology of MnO_2 (Figure 2c, 2e, and Figures S2, S4). In contrast to Amo-MnO_2, which lacks any crystalline characteristics, a lattice space of 0.34 nm was identified in L-Cry-MnO_2 (Figure 2e), indexed to the (002) plane of δ-MnO_2[39,40] (Figure 2d and Figure S5, Figure S6). These findings suggest that the crystallinity of Amo-MnO_2 was enhanced through annealing. The STEM-EDS (Figure 2f and Figures S3, S4) images display a uniform distribution of Mn and O throughout both samples, and the Mn/O atomic ratio was increased from 0.88 to 1.35 after annealing. This phenomenon

https://doi.org/10.1021/jacs.4c05512
J. Am. Chem. Soc. 2024, 146, 18639−18649

can be explained by the evaporation of adsorbed water in the annealing process.

The structure of MnO_2 electrocatalysts was further characterized by X-ray diffraction (XRD). As shown in Figure 3a, besides the characteristic peaks of graphite carbon from the CFP substrate (26.4°, 54.5°, etc., labeled with ♦), the broad diffraction peaks (labeled with ●) from Amo-MnO_2[41] were identified, manifesting its amorphous nature. In comparison, new diffraction peaks with low intensity (labeled with *) were observed from L-Cry-MnO_2, showcasing its improved crystallinity, consistent with the STEM results. Furthermore, the oxidation states of Mn in Amo-MnO_2 and L-Cry-MnO_2 were revealed by X-ray photoelectron spectroscopy (XPS). The average oxidation state (AOS) of Mn was calculated based on the splitting energy of Mn 3s peaks (Figure 3b and eq 2 in SI).[42,43] Amo-MnO_2 exhibits an AOS of 3.6, whereas L-Cry-MnO_2 shows a lower AOS of 3.3 (Table S1). The Mn 2p spectra further confirmed the AOS differences between Amo-MnO_2 and L-Cry-MnO_2. In the Mn 2p spectrum, the distance (ΔE $2p_{1/2}$) between Mn $2p_{1/2}$ (~653 eV) and the corresponding satellite peak (670 to 659 eV) has been employed to identify Mn oxidation states.[44,45] A decreased ΔE $2p_{1/2}$ value in L-Cry-MnO_2 suggests a lower Mn oxidation state. In Amo-MnO_2, the ΔE $2p_{1/2}$ value was 11.5 eV, while it was 11.0 eV in L-Cry-MnO_2, aligning well with the Mn 3s results (Figure S7 and Table S1). Moreover, the O 1s spectrum of Amo-MnO_2 (Figure 3c) was deconvoluted into three peaks: Mn−O−Mn (530.1 eV) from tetravalent MnO_2, Mn−OH (531.4 eV) from trivalent MnOOH, and adsorbed water (H−O−H bond, 532.8 eV).[43] Compared to Amo-MnO_2, the Mn−O−Mn to Mn−OH ratio decreased from 3.98 to 3.16 in L-Cry-MnO_2 as shown in Table S2. This difference sheds light on the cause behind the decreased Mn AOS in L-Cry-MnO_2.

The structures of Amo-MnO_2 and L-Cry-MnO_2 were further examined by Raman spectroscopy. The Raman bands of Amo-MnO_2 and L-Cry-MnO_2 can be divided into two areas: the intrinsic vibration modes (200−700 cm^{-1}) and the overtone vibrational modes (800−1400 cm^{-1}) (Figure S8).[46] Three

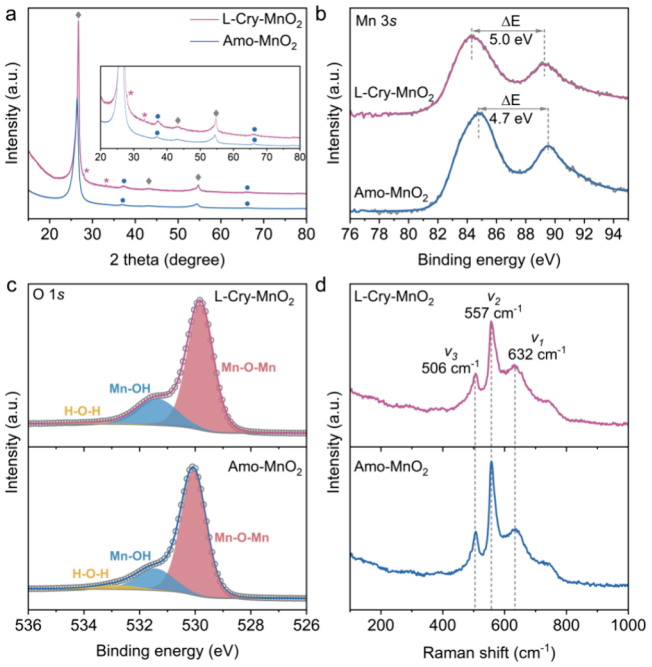

Figure 3. (a) X-ray diffraction patterns, (b) Mn 3s XPS spectra, (c) O 1s XPS spectra, and (d) Raman spectra of Amo-MnO_2 and L-Cry-MnO_2.

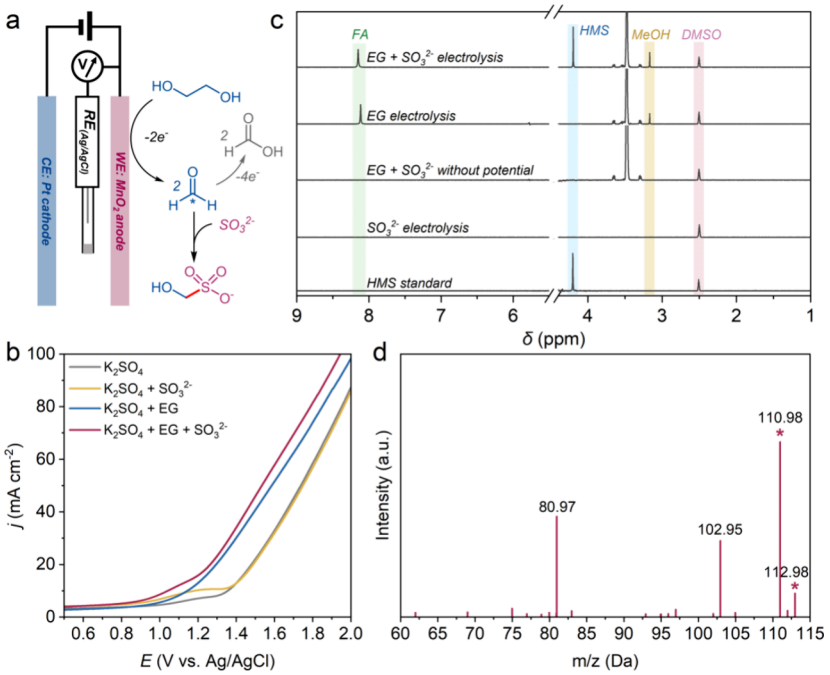

Figure 4. (a) Scheme of EGOR and C−S coupling reactions on MnO_2 anode in an undivided cell. (b) LSV curves at a scan rate of 10 mV s^{-1} in an undivided cell with Amo-MnO_2, platinum (Pt), and Ag/AgCl, as working, counter, and reference electrodes, respectively, with the addition of 150 mM EG and/or 15 mM Na_2SO_3. (c) ^1H NMR spectra of control experiments after electrolysis at 1.30 V vs Ag/AgCl for 2 h, with the addition of 150 mM EG and/or 15 mM Na_2SO_3. (d) ESI-MS spectrum of the electrolyte after electrolysis at 1.25 V vs Ag/AgCl for 18 h. The characteristic peaks of HMS are indicated by *.

https://doi.org/10.1021/jacs.4c05512
J. Am. Chem. Soc. 2024, 146, 18639−18649

Table 1. List of Control Experiments[a]

Entry	C-source	S-source	Electrolyte	E/V vs Ag/AgCl	HMS FE (%)	HMS yield rate (mmol cm^{-2} h^{-1})
1	EG	SO_3^{2-}	0.1 M K_2SO_4	1.3	58.8	0.22
2	EG	×	0.1 M K_2SO_4	1.3	×	×
3	×	SO_3^{2-}	0.1 M K_2SO_4	1.3	×	×
4	EG	SO_3^{2-}	0.1 M K_2SO_4	×	×	×
5	EG	HSO_3^-	0.1 M K_2SO_4	1.3	58.1	0.16
6	MeOH	SO_3^{2-}	0.1 M K_2SO_4	1.3	29.9	0.025
7	Gly	SO_3^{2-}	0.1 M K_2SO_4	1.3	47.9	0.23
8	EG	SO_3^{2-}	0.1 M Na_2SO_4	1.3	53.1	0.19
9	EG	SO_3^{2-}	0.25 M K_2SO_4	1.3	47.8	0.19
10	EG	SO_3^{2-}	0.05 M K_2SO_4	1.3	54.8	0.19

[a]× indicates the missing of one source/bias or that no HMS is produced. The reaction mechanisms of HMS formation with SO_3^{2-} and HSO_3^- as nucleophiles were demonstrated in Figure S25.

dominant peaks, v_1 to v_3, can be identified in the range of 200−700 cm^{-1} (Figure 3d). To elaborate, the frequency range of v_1 (620 cm^{-1} to 650 cm^{-1}) is linked to Mn−O stretching vibrations that are perpendicular to the sheet of MnO_6 octahedra and symmetric stretching of the Mn−O bond within the MnO_6 octahedra unit, while v_2 (570 and 590 cm^{-1}) signifies the Mn−O stretching vibration occurring within the plane of MnO_6 octahedra.[46−49] Compared to the previously reported Raman spectra of fine-crystalline MnO_2, such as α-MnO_2,[50] γ-MnO_2,[51] and δ-MnO_2,[49] a significant blue shift of the v_2 band is observed in both Amo-MnO_2 and L-Cry-MnO_2. This shift is attributed to the structural distortions in both samples, verifying their amorphous characteristics.

Electrocatalytic EGOR and C−S Formation. In a typical electrocatalytic PET upcycling process, PET usually undergoes a base-catalyzed hydrolysis to release EG and terephthalate (TPA) monomers. Subsequently, EG will be electrochemically oxidized while TPA remains unchanged. Hydrolysis usually happens under strong alkaline conditions, such as 1.0 M KOH. Therefore, the C−S coupling reaction was first conducted in 1.0 M KOH. As shown in Figure S9, after 2 h coelectrolysis of EG (C source) and SO_3^{2-} (S source) with Amo-MnO_2, HMS was not produced while only formic acid (FA) and glycolic acid were generated. To exclude the likelihood that Amo-MnO_2 might not be an optimal catalyst under alkaline conditions, a Cu-deposited Ni Foam ($NiCu_{60s}$/NF), which has been recently reported as an efficient EGOR catalyst under highly alkaline conditions,[52] was employed for the C−S coupling. Similarly, with the $NiCu_{60s}$/NF catalyst, only FA and methanol (MeOH) were detected as the C−S coupling products (Figure S10). These results indicate that the EGOR to the formic acid pathway under alkaline environments is more advantageous, whereas the C−S coupling is completely suppressed (Figure S11). Alternatively, near-neutral conditions (0.1 M K_2SO_4, pH, 5.65) were employed to accomplish the C−S bond formation.

Before directly upcycling PET plastics, linear sweep voltammetry (LSV) of Amo-MnO_2 catalyst in 0.1 M K_2SO_4 solution was evaluated toward OER, EGOR, and the C−S coupling (Figure 4a and 4b). Compared to OER, with an addition of 150 mM EG, a potential reduction of 185 mV (to reach 20 mA cm^{-2}) was observed (Figure 4b), indicating that Amo-MnO_2 is more selective toward EGOR than OER. With the addition of Na_2SO_3, the LSV only shifts slightly, indicating Na_2SO_3 is stable under electrochemical conditions, and the C−S coupling might be a chemical reaction. As a control, L-Cry-MnO_2 exhibits a similar potential reduction comparable to Amo-MnO_2 across OER, EGOR, and C−S coupling reactions (Figure S12).

Furthermore, the C−S coupling was performed through coelectrolysis of EG (C source) and Na_2SO_3 (S source) under chronoamperometry conditions (i−t) for 2 h. As shown in Figure 4c, HMS was identified as the main C−S coupling product from the ^{1}H NMR spectra. The formation of HMS was further verified and validated through the ESI-MS analysis (Figure 4d and Figure S13) and the control experiments (Figure 4c and Table 1). From the control experiments, HMS was absent without the presence of EG, Na_2SO_3, or applied potential (Table 1). This result provides compelling proof that HMS is formed by combining the intermediates generated in the EGOR with SO_3^{2-}. It is worth noting that HMS, industrially produced from reacting formaldehyde with sodium bisulfite, is an important raw material and intermediate widely used in organic synthesis, pharmaceuticals, and agrochemicals.[16] For instance, HMS has been applied to prepare oil-soluble additives[53] to improve lubricant oil's anticorrosive, dispersant, and antioxygenic properties. Meanwhile, HMS can be used as a textile stripping agent, a fixing agent for keratin-containing fibers, and a preservative in cosmetics.

Interestingly, in both EGOR and C−S coupling processes, besides the common major products, formic acid (FA) and HMS, a small amount of (∼1.2% of FE at 1.40 V vs Ag/AgCl) MeOH was identified as a minor product. In an undivided cell, the anodic products, like formaldehyde, can easily diffuse from the anode to the cathode for further reactions. Therefore, we propose that MeOH could be produced through two distinct means: (1) the well-known Cannizzaro reaction[28,54−56] in which two formaldehyde molecules disproportionate to form MeOH and formic acid, and (2) the cathodic reduction of EGOR intermediates (i.e., formaldehyde) or its products (i.e., formic acid) (Figure S14). It is worth noting that the Cannizzaro reaction is base-catalyzed. Nevertheless, electrolysis reactions were conducted under near-neutral conditions in this work. We hypothesize that the Cannizzaro reaction took place at the cathode, where the hydrogen evolution reaction (HER) generates a localized alkaline environment close to the cathode surface to initialize the diffused aldehyde disproportionation. A similar phenomenon was first reported by Marc T. M. Koper's group for CO_2 reduction.[56] To investigate the origin of the small amount of MeOH, EGOR and C−S coupling reactions were carried out in a divided cell (Figure S14, see SI for more details). When EGOR and C−S coupling reactions were respectively conducted in the anodic chamber, MeOH was not observed in both reactions (Figure S15). This result suggests that MeOH is

https://doi.org/10.1021/jacs.4c05512
J. Am. Chem. Soc. 2024, 146, 18639−18649

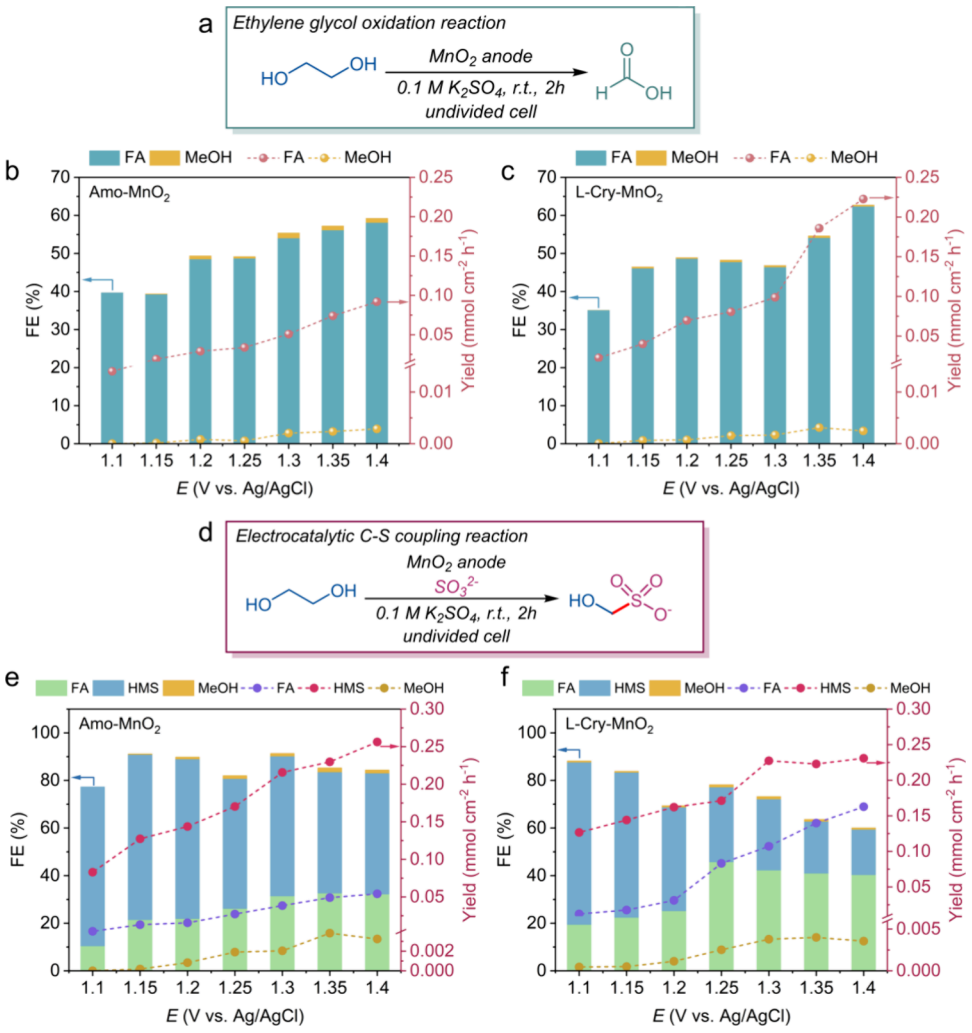

Figure 5. (a) Scheme of electrocatalytic EGOR. FEs and yields of products at potentials ranging from 1.1 to 1.4 V vs Ag/AgCl with (b) Amo-MnO_2 and (c) L-Cry-MnO_2 as catalysts, respectively. Herein, only 150 mM EG was added into the electrolyte as the C source. (d) Scheme of electrocatalytic C−S coupling reaction. FEs and yields of products at potentials ranging from 1.1 to 1.4 V vs Ag/AgCl with (e) Amo-MnO_2 and (f) L-Cry-MnO_2 as catalysts, respectively. 150 mM EG and 15 mM Na_2SO_3 were added into the electrolyte as the C and S sources, respectively.

generated from the EGOR intermediate species transitioning from the anode to the cathode. In addition, to investigate whether FA can be converted to MeOH on the cathode, pure FA was introduced into the cathodic chamber in the divided cell. However, no MeOH was produced after EGOR and C−S coupling (Figure S16), indicating that converting FA into MeOH is unfeasible. These results demonstrate that MeOH is generated via the Cannizzaro reaction or reduction of diffused intermediates on the cathode. Unfortunately, these two reactions are indistinguishable from the experimental perspective.

Furthermore, the potential-dependent EGOR and C−S coupling reactions were conducted, respectively. First, in EGOR (Figure 5b to 5c), the FEs and yields of FA and MeOH display an increased trend with an elevated bias on both Amo-MnO_2 and L-Cry-MnO_2. Furthermore, the product selectivity toward FA (FE, 48.7% at 1.25 V vs Ag/AgCl) on Amo-MnO_2 is comparable to that on L-Cry-MnO_2 (47.7% at 1.25 V vs Ag/AgCl). Nevertheless, L-Cry-MnO_2 shows a much greater FA yield, suggesting that L-Cry-MnO_2 assists in converting EG to FA. For the C−S coupling reaction (Figure S19), as shown in Figure 5e to 5f, the FEs of FA and HMS both display strong potential-dependent relationships. With an increased potential, the FE of FA shows an elevated trend; in contrast, the FE of HMS was gradually reduced. This reversed trend observed in FE between FA and HMS can be attributed to the rapid oxidization of EG to FA at an elevated bias, leading to a shorter lifespan of the formaldehyde intermediate and decreased efficiency in the C−S coupling process. In contrast to Amo-MnO_2, L-Cry-MnO_2 demonstrates greater selectivity toward FA production under identical reaction conditions. This aligns with the results from the EGOR study, which shows that low-crystalline MnO_2 promotes the production of FA while suppressing the C−S coupling reaction. Therefore, the selectivity of HMS on Amo-MnO_2 (i.e., FE of HMS, 67% at 1.2 V vs Ag/AgCl) is typically higher compared to that on L-Cry-MnO_2 (i.e., FE of HMS, 44% at 1.2 V vs Ag/AgCl). It is important to mention that the total selectivity of the C−S coupling reaction (FE_{total}, 89.8% at 1.2 V vs Ag/AgCl) surpasses that of the EGOR (FE_{total}, 49.4% at 1.2 V vs Ag/AgCl). This result is rare compared to previous C−X coupling studies, where the selectivity of electro-reduction/oxidation of C sources is usually higher than that of the C−X coupling reaction. For example, we have previously discussed how methylamine can be

https://doi.org/10.1021/jacs.4c05512
J. Am. Chem. Soc. 2024, 146, 18639−18649

produced by coreducing CO_2 and NO_3^-. In the study, the selectivity for CO_2 reduction (FE is ~70% for various products) and NO_3^- reduction (FE is ~30% for NH_3 production) were significantly greater than the selectivity for producing C−N product, methylamine (with an optimal 13% FE).[10] In general, this can be attributed to the strong electrostatic interaction between SO_3^{2-} and anode enriches SO_3^{2-} nucleophiles, which can rapidly intercept the EGOR intermediates and drive the EGOR equilibrium forward to produce more stable intermediates.

Moreover, the concentration effects of EG and Na_2SO_3 were investigated. With the fixed EG concentration (150 mM), the HMS's FE and yield were elevated with an increased Na_2SO_3 concentration (7.5 mM to 15 mM) (Figure S20 and Figure S21). Meanwhile, at a constant concentration of Na_2SO_3 (15 mM), an increased EG concentration (from 75 mM, 150 mM to 300 mM) induced an enhanced HMS yield. Interestingly, in terms of HMS's FE, there is no clear trend when the concentration of EG is elevated. For instance, at 1.1 V, FE is increased with an increased EG concentration (from 75 mM to 300 mM). However, at 1.2 V, an opposite FE trend is observed. Herein, the best selectivity (FE = ~85%) for HMS production was achieved at 1.1 V (with 300 mM EG and 15 mM SO_3^{2-}). As we discussed earlier, capturing electrophilic C active intermediates from CO_2 reduction to construct C−S bond compounds via nucleophilic attack usually suffers from low selectivity. In comparison, mining C resources from electro-oxidative plastic upcycling is beneficial due to the following reasons: First, oxidative coupling reaction can easily outperform reductive coupling reaction since the SO_3^{2-} anion tends to be attracted to the anode. In contrast, the nucleophile will be repelled by the negatively charged cathode. If the intermediates are surface adsorbed, the selectivity and efficiency in generating a C−S compound will be further reduced. Second, CO_2 needs to be captured and concentrated in electrolyte before electrocatalysis. Due to its limited solubility in the aqueous solution, a gas-diffusion electrode needs to be employed. In comparison, hydrolysis is a common chemical recycling approach for PET plastic wastes, and a high concentration of PET monomers (C source) can be efficiently obtained after the initial treatment.

To expand the substrate scope, MeOH (C_1) (Figure S22) and glycerol (C_3) (Figure S23) were further employed for C−S coupling. When MeOH is employed as the C source, the FE and yield of HMS are much lower than that of EG, with a maximum FE of 31% and yield of 0.027 mmol cm^{-2} h^{-1} (Figure S22). However, when glycerol is applied, the FE and yield of HMS are comparable to that of EG (Figure S23). In addition, to expand the nucleophile scope, $NaHSO_3$ was further employed as the S source. In this case, similar to utilizing SO_3^{2-}, HMS was identified as the primary C−S coupling product. However, the FE and yield of HMS are slightly lower (Figure S24), possibly due to the reduced nucleophilicity of HSO_3^- as compared to SO_3^{2-}. As well, the electrolyte effects (cations and concentration) were investigated (Figures S26 to S28 and Table 1). Under various electrolytes (0.1 M Na_2SO_4, 0.05 M K_2SO_4, 0.1 M K_2SO_4, and 0.25 M K_2SO_4) conditions, both FE and yield of HMS exhibit comparable results. These results indicate the resilience of the MnO_2 catalyst to various cations and concentrations of electrolytes when catalyzing C−S bond formation. Moreover, it is important to note that the EG monomer can not only be extracted from wasted plastics but also be sourced from biomass resources. Additionally, some other alcohols derived from biomass, like MeOH, and glycerol can be used as substrates for C−S coupling as well. Thus, the success of this strategy can benefit not only plastic upcycling but also biomass upconversion.

In addition, the stability of Amo-MnO_2 was further evaluated. From the SEM images (Figures S29 and S30), the dense coverage of MnO_2 on CFP was observed after 2 h EGOR and C−S coupling reactions. Even after an 18 h C−S reaction, no drop-off or morphology changes of MnO_2 were found (Figure S31). The XPS survey spectra (Figures S32 and S33) of Amo-MnO_2 after reactions show identical patterns as those of original Amo-MnO_2. In addition, analysis of high-resolution XPS spectra reveals that the oxidation states of Mn remained nearly unchanged compared to those before electrolysis (Tables S3 and S4). Finally, the identical Raman spectra of Amo-MnO_2 before and after electrolysis provide additional evidence for the exceptional long-term stability of Amo-MnO_2 (Figure S34).

Mechanistic Investigation: In-Situ Raman for Identifying Catalyst's Active Sites. To identify active sites of Amo-MnO_2 during electrocatalysis, in situ Raman was conducted for OER, EGOR, and C−S coupling reactions, respectively (Figures S35−37, in situ Raman section in SI). Under OER conditions (in 0.1 M K_2SO_4) (Figure S38), the sharp peak located at 968 cm^{-1} is ascribed to the binding of SO_4^{2-} to the catalyst surface. The peaks in the region from 450 to 750 cm^{-1} are assigned to the stretching vibrations of MnO_6 octahedra, labeled with v_1 to v_3. Herein, v_2 (559 cm^{-1}) and v_3 (495 cm^{-1}) peak positions remained unchanged when the applied potentials were elevated from 1.0 to 1.30 V as under the open circuit potential (OCP). However, the v_1 vibration was gradually broadened with an increased bias, which could be attributed to an increased degree of Jahn−Teller distortion during the anodic process.[46]

Further, the in-situ Raman experiment was conducted under EGOR conditions. As shown in Figure 6a, the characteristic stretching vibration peaks of MnO_6 octahedra were observed in the region of 450 cm^{-1} to 750 cm^{-1}. In comparison with the OER condition, a blue shift of the v_1 band and a red shift of the v_2 band were observed, implying that the adsorption of EG molecules on the surface of MnO_2 led to alterations in the Mn−O bond length. Meanwhile, with the further addition of SO_3^{2-} for the C−S coupling reaction, a much lower v_1 band (at 615 cm^{-1}) was observed (Figure 6b). This phenomenon indicates that the simultaneous adsorption of EG and SO_3^{2-} on MnO_6 octahedra modifies the Mn−O stretching vibration. In addition, with an elevated anodic potential, the peak at 854 cm^{-1}, which corresponds to the adsorbed EG molecules, decreased steadily while the 1040 cm^{-1} peak, reflecting the formation of carbonate (CO_3^{2-}),[57] emerged. The disappearance of EG and the appearance of CO_3^{2-} indicate that EG can be finally oxidized to carbonate at the electrode's surface.[58] Overall, the above results show that the original structure of Amo-MnO_2 is intact under EROR and C−S coupling reactions.

Density Functional Theory Computations: Active Intermediates Species Identification. Density functional theory (DFT) calculation was further performed to investigate the possible EGOR intermediates and C−S coupling reaction mechanism. First, to test if the solution-based formaldehyde (HCHO) intermediates react with SO_3^{2-}, formaldehyde was directly added as the C-source into the Na_2SO_3 solution for the C−S coupling reaction without MnO_2 catalyst or applying potential. Nevertheless, HMS was not able to be identified after a 21 h reaction under room temperature (Figure S39). This result indicates that solution-based formaldehyde is inactive to couple with SO_3^{2-} for the formation of the C−S bond.

https://doi.org/10.1021/jacs.4c05512
J. Am. Chem. Soc. 2024, 146, 18639−18649

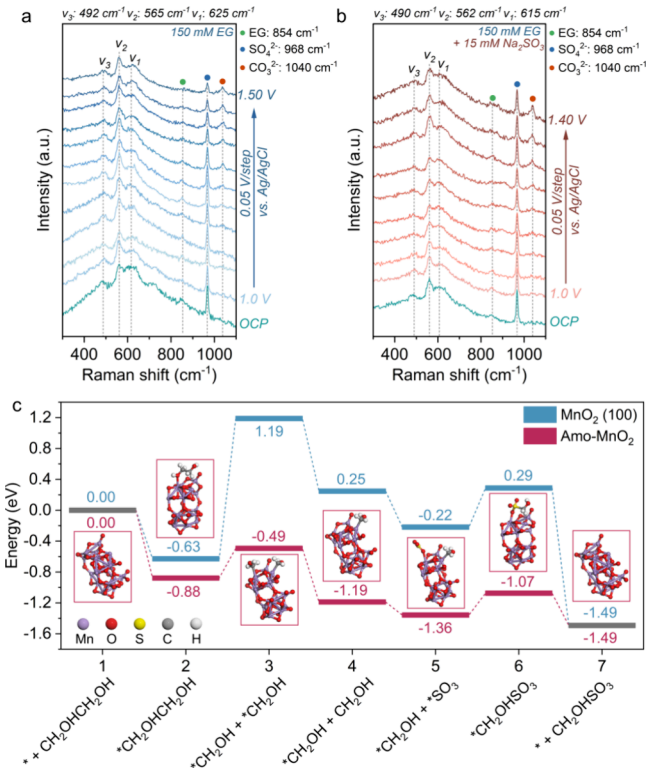

Figure 6. In-situ Raman spectra of Amo-MnO_2 for (a) EG oxidation and (b) C−S coupling reactions. (c) Energy diagram for the key reaction pathways and intermediates during the C−S coupling reaction on Amo-MnO_2. The inset was the optimized intermediate adsorption configurations on Amo-MnO_2.

Therefore, the possible active intermediates are surface-adsorbed electrophiles (*CH_2OH, *CHOH, and *COH) that are in situ generated from EGOR. Within the range of potential intermediates, after the C−S coupling step, *CHOH and *COH require hydrogenation steps to form HMS, which are thermodynamically unfeasible under electrooxidation conditions. Thus, only *CH_2OH was calculated as an intermediate. In terms of understanding the benefits of amorphous phase MnO_2 for C−S coupling, the crystalline MnO_2 (100) slab was applied as a control in DFT calculation. As shown in Figure 6c, the EG adsorption on crystal MnO_2 (100) and Amo-MnO_2 was calculated to be exothermic. However, Amo-MnO_2 is more beneficial than MnO_2 (100) for EG adsorption, indicated by a smaller energy difference (ΔE, −0.63 eV) on MnO_2 (100). In addition, the EG C−C bond cleavage process, generating the key *CH_2OH intermediate, was determined to be the rate-determining step (RDS) for both catalysts (Figure S40). Compared to MnO_2 (100) (ΔE of RDS, 1.82 eV), the ΔE of RDS was significantly reduced (0.39 eV) on Amo-MnO_2. This result demonstrates that Amo-MnO_2 is more advantageous than its crystalline form when it comes to generating the key intermediate. Subsequently, the *CH_2OH intermediate is directly coupled with adsorbed sulfur species (*SO_3) to form the C−S bond. The ΔE for the C−S coupling step on Amo-MnO_2 was calculated to be 0.29 eV, which is again lower than that of MnO_2 (100) (0.51 eV). Moreover, DFT calculation reveals the electron density differences between Amo-MnO_2 and MnO_2 (100). As shown in Figure S41, when *CH_2OH is adsorbed on the Amo-MnO_2, the valence state of C was calculated to be −0.53 which is more negative than that of MnO_2 (100) (−0.41), signifying that more electrons can be transferred to the adsorbed species from Amo-MnO_2 than MnO_2 (100), which is beneficial for activating EG. Simultaneously, a much shorter Mn−C bond length on Amo-MnO_2 (1.992) manifests stronger EG adsorption on Amo-MnO_2 in comparison with MnO_2 (100) (Mn−C, 2.150). These results reveal the RDS step in C−S coupling and the benefits of amorphous MnO_2 compared to the crystalline phase for C−S bond formation.

Electrocatalytic Real-World PET Plastic Wastes Upcycling to HMS. To explore the practical application of this method for real-world plastic waste upcycling, commercial PET powder and water bottles were employed for HMS electrosynthesis (Figure 7a). PET powder was first hydrolyzed in 2.0 M KOH (Figure S42 and Figure S43). After hydrolysis, the hydrolysate was adjusted to pH = 3.0 (Figure S45) to precipitate TPA. Following the isolation of the precipitated TPA (Figure 7b and Figure S46), the hydrolysate (Figure S47) pH was adjusted to ∼5.65 and directly employed for the C−S coupling reaction (step 4 in Figure 7b). FA and HMS were detected as the main products (Figure S49) after electrolysis. Just like EG as a substrate, the FE of HMS was decreased as the potential increased from 1.1 to 1.4 V with a maximum FE (∼65%) achieved at 1.1 V. Simultaneously, the yield of HMS was enhanced with an increased bias (Figure 7d). Furthermore, a commercial PET water bottle was pretreated in 2.0 M KOH followed by TPA precipitation, separation, and pH adjustment before the C−S coupling. Compared to commercial PET powder, lower concentrations of monomers (EG and TPA) were observed (Figures 7b, S43, S45, and S47). This result can be explained by the fact that commercial PET bottles are usually more resistant under hydrolysis conditions to meet industrial requirements. When the PET bottle hydrolysate was directly applied for the C−S coupling reaction, ∼45%−65% FEs of HMS were achieved after 2 h electrolysis (Figure 7e and Figure S49), comparable to the efficiency and selectivity obtained from directly employing EG or PET powder hydrolysate. An examination of the technoeconomics (TEA, Figure S50) reveals that greater profitability ($2568.2) per ton of HMS production can be achieved through the electrocatalytic PET waste upcycling approach, as opposed to the conventional HMS manufacturing process (net profit = $1929.4). Additionally, the profit stemming from PET waste upcycling to FA falls below the levelized costs (net profit = −$5952), potentially due to the poor selectivity and efficiency of Amo-MnO_2 in FA production.

CONCLUSION

In this work, we developed a novel plastic waste upcycling strategy to construct C−S compounds via coupling PET plastic wastes with sulfur oxides in an aqueous solution. A cost-effective amorphous MnO_2 (Amo-MnO_2) was synthesized as a catalyst through a facile electrodeposition method. The Amo-MnO_2 is capable of oxidizing PET plastic-derived EG under near-neutral conditions, which allows stabilization of the active C electrophile intermediates during the PET upcycling process for the C−S coupling reaction. Thus, HMS can be efficiently synthesized with up to ∼70% FE. In addition, this PET waste upcycling method displays excellent substrate compatibility. HMS was successfully produced with C_1 (MeOH) and C_3 (glycerol) biomass-derived compounds. Moreover, this strategy was applied to upcycling real-world plastic waste. With the addition of sulfur oxides into PET waste hydrolysates, HMS was selectively synthesized with FE up to ∼65%. Lastly, DFT calculations reveal that the C−C cleavage step of EG is the RDS,

https://doi.org/10.1021/jacs.4c05512
J. Am. Chem. Soc. 2024, 146, 18639−18649

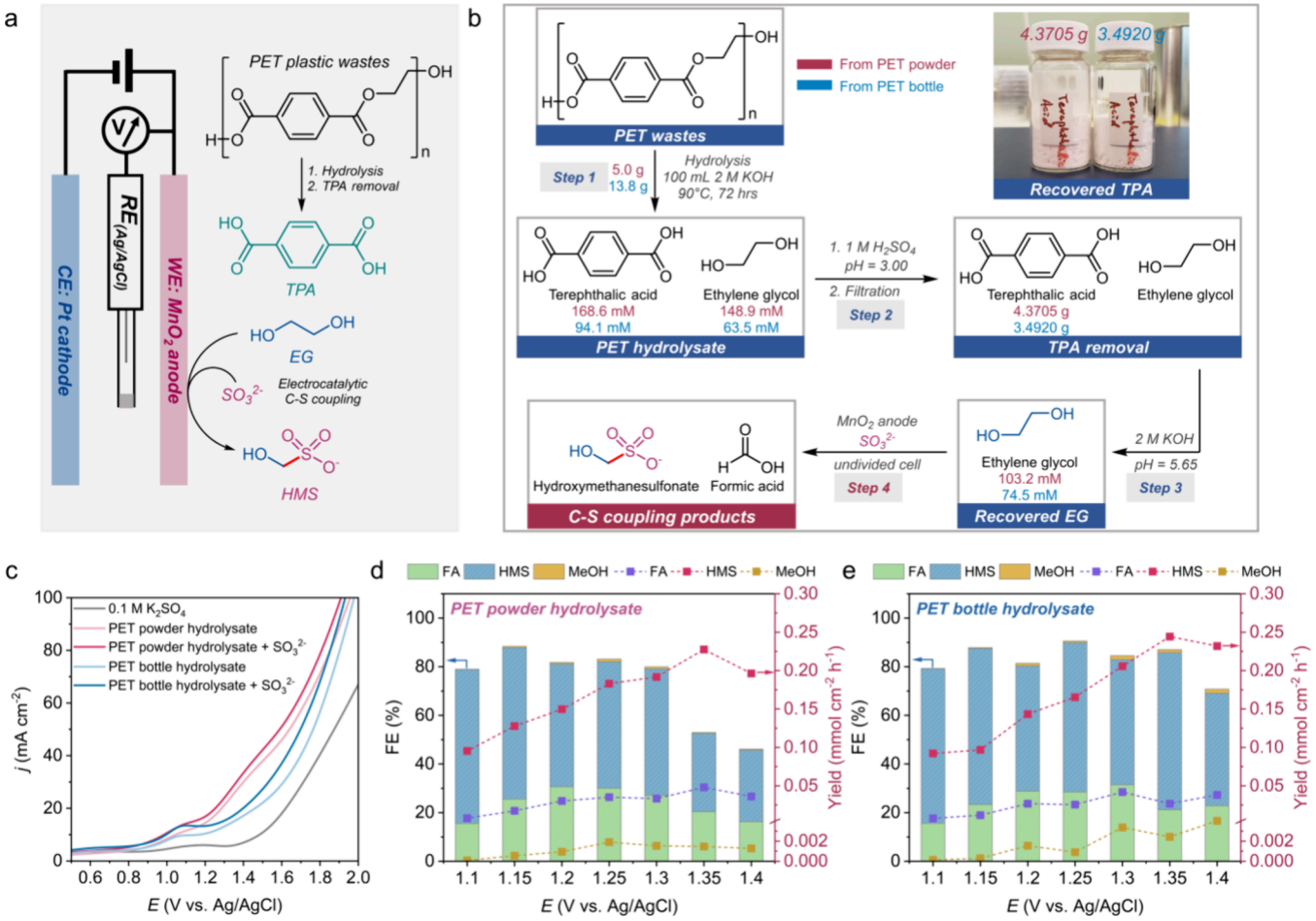

Figure 7. (a) Scheme of electrocatalytic PET plastic wastes to HMS. (b) Commercial PET powder and PET water bottle upcycling pathways, the inset image represents the recovered TPA. 5 g of PET powder was hydrolyzed in 2.0 M KOH. After hydrolysis, the hydrolysate was adjusted to pH = 3.0 to precipitate TPA. 4.3705 g of TPA (purity, 72.2%) was recovered and isolated, leaving 103.2 mM of EG after adjusting the filtrate pH to 5.65. The remaining hydrolysate was directly employed with the addition of Na_2SO_3 (15 mM) for the C−S coupling reaction. For the PET water bottle (13.8 g), only 3.4920 g of TPA (purity, 58.9%) was recovered and the EG concentration was 74.5 mM. (c) LSV curves under OER, PET plastic waste hydrolysates with and without the addition of SO_3^{2-} (15 mM). Products FE and yield with (d) PET powder and (e) PET bottle hydrolysates as substrates, respectively.

and the amorphous nature of MnO_2 can significantly reduce the energy barrier of the RDS and C−S coupling step compared to its crystal analog. Over the last century, humans have managed to mine raw materials, increase their value, and manufacture new products from those materials. Mining plastic waste would open a new avenue for us to recover resources through reinserting value-added chemicals into the supply chain and mitigate the potential environmental issues and economic impacts of plastic waste.

■ ASSOCIATED CONTENT

Supporting Information

The Supporting Information is available free of charge at https://pubs.acs.org/doi/10.1021/jacs.4c05512.

SEM images, STEM images, EDS, and LSV curves of Amo-MnO_2 and L-Cry-MnO_2. Reaction condition optimization. In-situ Raman section. ESI-MS spectra of synthesized HMS and PET plastic wastes hydrolysates. Optimized DFT-computed catalysts' structures. Amo-MnO_2 stability evaluation. Real-world PET plastic wastes upcycling. (PDF)

■ AUTHOR INFORMATION

Corresponding Author

Jing Gu − *Department of Chemistry and Biochemistry, San Diego State University, San Diego, California 92182, United States;* orcid.org/0000-0002-5506-0049; Email: jgu@sdsu.edu

Authors

Hongxing Kang − *Department of Chemistry and Biochemistry, San Diego State University, San Diego, California 92182, United States*

Dong He − *Department of Physics, Wuhan University, Wuhan, Hubei 430072, China*

Christopher Turchiano − *Department of Chemistry and Biochemistry, San Diego State University, San Diego, California 92182, United States;* orcid.org/0000-0003-3173-3795

Xingxu Yan − *Department of Materials Science and Engineering, University of California, Irvine, California 92697, United States;* orcid.org/0000-0001-7991-4849

Jingtong Chai − *Department of Chemistry and Biochemistry, San Diego State University, San Diego, California 92182, United States*

https://doi.org/10.1021/jacs.4c05512
J. Am. Chem. Soc. 2024, 146, 18639−18649

Melanie Weed − *Department of Chemistry and Biochemistry, San Diego State University, San Diego, California 92182, United States*
Gregory I. Elliott − *Department of Chemistry and Biochemistry, San Diego State University, San Diego, California 92182, United States*
David Onofrei − *Department of Chemistry and Biochemistry, San Diego State University, San Diego, California 92182, United States*
Xiaoqing Pan − *Department of Materials Science and Engineering, University of California, Irvine, California 92697, United States; Department of Physics and Astronomy, University of California, Irvine Irvine, California 92697, United States*
Xiangheng Xiao − *Department of Physics, Wuhan University, Wuhan, Hubei 430072, China;* orcid.org/0000-0001-9111-1619

Complete contact information is available at: https://pubs.acs.org/10.1021/jacs.4c05512

Notes

The authors declare no competing financial interest.

■ ACKNOWLEDGMENTS

We acknowledge the use of facilities and instrumentation at the UC Irvine Materials Research Institute (IMRI), which is supported in part by the National Science Foundation through the UC Irvine Materials Research Science and Engineering Center (DMR-2011967). J.G. acknowledges the financial support received for this research from NSF award CHE-2154837.

■ REFERENCES

(1) Nielsen, T. D.; Hasselbalch, J.; Holmberg, K.; Stripple, J. Politics and the plastic crisis: A review throughout the plastic life cycle. *WIREs Energy Environ* **2020**, *9*, No. e360.
(2) McGuirk, C. M.; Bazilian, M. D.; Kammen, D. M. Mining Plastic: Harvesting Stored Energy in a Re-use Revolution. *One Earth* **2019**, *1*, 392−394.
(3) Geyer, R.; Jambeck, J. R.; Law, K. L. Production, use, and fate of all plastics ever made. *Sci. Adv.* **2017**, *3*, No. e1700782.
(4) *The New Plastics Economy: Rethinking the future of plastics & catalysing action*; Ellen MacArthur Foundation: 2017.
(5) Yan, Y.; Zhou, H.; Xu, S.-M.; Yang, J.; Hao, P.; Cai, X.; Ren, Y.; Xu, M.; Kong, X.; Shao, M.; Li, Z.; Duan, H. Electrocatalytic Upcycling of Biomass and Plastic Wastes to Biodegradable Polymer Monomers and Hydrogen Fuel at High Current Densities. *J. Am. Chem. Soc.* **2023**, *145*, 6144−6155.
(6) Rooney, C. L.; Wu, Y.; Tao, Z.; Wang, H. *J. Am. Chem. Soc. J. Am. Chem. Soc.* **2021**, *143*, 19983−19991.
(7) Li, J.; Kornienko, N. Electrochemically driven C−N bond formation from CO_2 and ammonia at the triple-phase boundary. *Chem. Sci.* **2022**, *13*, 3957−3964.
(8) Saravanakumar, D.; Song, J.; Lee, S.; Hur, N. H.; Shin, W. Electrocatalytic Conversion of Carbon Dioxide and Nitrate Ions to Urea by a Titania−Nafion Composite Electrode. *ChemSusChem* **2017**, *10*, 3999−4003.
(9) Li, J.; Al-Mahayni, H.; Chartrand, D.; Seifitokaldani, A.; Kornienko, N. Electrochemical formation of C−S bonds from CO_2 and small-molecule sulfur species. *Nat. Synth.* **2023**, *2*, 757−765.
(10) Wu, Y.; Jiang, Z.; Lin, Z.; Liang, Y.; Wang, H. Direct electrosynthesis of methylamine from carbon dioxide and nitrate. *Nat. Sustainability* **2021**, *4*, 725−730.
(11) Nascimento, B.; Filho, G. R.; Frigoni, E. S.; Soares, H. M.; da Silva Meireles, C.; Cerqueira, D. A.; Valente, A. J. M.; de Albuquerque Carvalho, R.; de Assunção, R. M. N.; de Castro Motta, L. A. Application of cellulose sulfoacetate obtained from sugarcane bagasse as an additive in mortars. *J. Appl. Polym. Sci.* **2012**, *124*, 510−517.
(12) Seeponkai, N.; Wootthikanokkhan, J. Proton conductivity and methanol permeability of sulfonated poly(vinyl alcohol) membranes modified by using sulfoacetic acid and poly(acrylic acid). *J. Appl. Polym. Sci.* **2007**, *105*, 838−845.
(13) Gernon, M. D.; Wu, M.; Buszta, T.; Janney, P. Environmental benefits of methanesulfonic acid. Comparative properties and advantages. *Green Chem.* **1999**, *1*, 127−140.
(14) Balaji, R.; Pushpavanam, M. Methanesulphonic acid in electroplating related metal finishing industries. *Trans. IMF* **2003**, *81*, 154−158.
(15) Nacsa, E. D.; Lambert, T. H. Cyclopropenone Catalyzed Substitution of Alcohols with Mesylate Ion. *Org. Lett.* **2013**, *15*, 38−41.
(16) Makarov, S. V Recent trends in the chemistry of sulfur-containing reducing agents. *Russ. Chem. Rev.* **2001**, *70*, 885−895.
(17) Otocka, S.; Kwiatkowska, M.; Madalińska, L.; Kiełbasiński, P. Chiral Organosulfur Ligands/Catalysts with a Stereogenic Sulfur Atom: Applications in Asymmetric Synthesis. *Chem. Rev.* **2017**, *117*, 4147−4181.
(18) Gu, X.; Zhu, Y. Z. Therapeutic applications of organosulfur compounds as novel hydrogen sulfide donors and/or mediators. *Expert Rev. Clin. Pharmacol.* **2011**, *4*, 123−133.
(19) Walag, A. M. P.; Ahmed, O.; Jeevanandam, J.; Akram, M.; Ephraim-Emmanuel, B. C.; Egbuna, C.; Semwal, P.; Iqbal, M.; Hassan, S.; Uba, J. O. In *Health Benefits of Organosulfur Compounds. In Functional Foods and Nutraceuticals: Bioactive Components, Formulations and Innovations*; Egbuna, C., Dable Tupas, G., Eds.; Springer International Publishing: Cham, 2020; pp 445−472.
(20) Guo, W.; Wang, D.-Y.; Chen, Q.; Fu, Y. Advances of Organosulfur Materials for Rechargeable Metal Batteries. *Adv. Sci.* **2022**, *9*, 2103989.
(21) Pan, Z.; Brett, D. J. L.; He, G.; Parkin, I. P. Progress and Perspectives of Organosulfur for Lithium−Sulfur Batteries. *Adv. Energy Mater.* **2022**, *12*, 2103483.
(22) Sakakura, A.; Yamada, H.; Ishihara, K. Enantioselective Diels−Alder Reaction of α-(Acylthio)acroleins: A New Entry to Sulfur-Containing Chiral Quaternary Carbons. *Org. Lett.* **2012**, *14*, 2972−2975.
(23) Amri, N.; Wirth, T. Recent Advances in the Electrochemical Synthesis of Organosulfur Compounds. *Chem. Rec.* **2021**, *21*, 2526−2537.
(24) Reddy, R. J.; Kumari, A. H. Synthesis and applications of sodium sulfinates (RSO2Na): a powerful building block for the synthesis of organosulfur compounds. *RSC Adv.* **2021**, *11*, 9130−9221.
(25) Arisawa, M.; Yamaguchi, M. Transition-metal-catalyzed synthesis of organosulfur compounds. *Pure Appl. Chem.* **2008**, *80*, 993−1003.
(26) Savateev, A.; Kurpil, B.; Mishchenko, A.; Zhang, G.; Antonietti, M. A "waiting" carbon nitride radical anion: a charge storage material and key intermediate in direct C−H thiolation of methylarenes using elemental sulfur as the "S"-source. *Chem. Sci.* **2018**, *9*, 3584−3591.
(27) Wang, Y.; Deng, L.; Mei, H.; Du, B.; Han, J.; Pan, Y. Electrochemical oxidative radical oxysulfuration of styrene derivatives with thiols and nucleophilic oxygen sources. *Green Chem.* **2018**, *20*, 3444−3449.
(28) Cannizzaro, S. Ueber den der Benzoësäure entsprechenden Alkohol. *Justus Liebigs Ann. Chem.* **1853**, *88* (88), 129−130.
(29) Li, J.; Li, L.; Ma, X.; Han, X.; Xing, C.; Qi, X.; He, R.; Arbiol, J.; Pan, H.; Zhao, J.; Deng, J.; Zhang, Y.; Yang, Y.; Cabot, A. Selective Ethylene Glycol Oxidation to Formate on Nickel Selenide with Simultaneous Evolution of Hydrogen. *Adv. Sci.* **2023**, *10*, 2300841.
(30) Zhou, H.; Ren, Y.; Li, Z.; Xu, M.; Wang, Y.; Ge, R.; Kong, X.; Zheng, L.; Duan, H. Electrocatalytic upcycling of polyethylene terephthalate to commodity chemicals and H_2 fuel. *Nat. Commun.* **2021**, *12*, 4679.
(31) Wang, J.; Li, X.; Zhang, T.; Chen, Y.; Wang, T.; Zhao, Y. Electro-Reforming Polyethylene Terephthalate Plastic to Co-Produce Valued

Chemicals and Green Hydrogen. *J. Phys. Chem. Lett.* **2022**, *13*, 622−627.
(32) Qi, J.; An, Z.; Li, C.; Chen, X.; Li, W.; Liang, C. Electrocatalytic selective oxidation of ethylene glycol: A concise review of catalyst development and reaction mechanism with comparison to thermocatalytic oxidation process. *Curr. Opin. Electrochem.* **2022**, *32*, 100929.
(33) Uekert, T.; Kasap, H.; Reisner, E. Photoreforming of Nonrecyclable Plastic Waste over a Carbon Nitride/Nickel Phosphide Catalyst. *J. Am. Chem. Soc.* **2019**, *141*, 15201−15210.
(34) Liu, F.; Gao, X.; Shi, R.; Guo, Z.; Tse, E. C. M.; Chen, Y. Concerted and Selective Electrooxidation of Polyethylene-Terephthalate-Derived Alcohol to Glycolic Acid at an Industry-Level Current Density over a Pd−Ni(OH)$_2$ Catalyst. *Angew. Chem., Int. Ed.* **2023**, *62*, No. e202300094.
(35) Du, M.; Zhang, Y.; Kang, S.; Xu, C.; Ma, Y.; Cai, L.; Zhu, Y.; Chai, Y.; Qiu, B. Electrochemical Production of Glycolate Fuelled By Polyethylene Terephthalate Plastics with Improved Techno-Economics. *Small* **2023**, *19*, 2303693.
(36) Lei, Z.; Wang, T.; Zhao, B.; Cai, W.; Liu, Y.; Jiao, S.; Li, Q.; Cao, R.; Liu, M. Recent Progress in Electrocatalysts for Acidic Water Oxidation. *Adv. Energy Mater.* **2020**, *10*, 2000478.
(37) Singh, A.; Spiccia, L. Water oxidation catalysts based on abundant 1st row transition metals. *Coord. Chem. Rev.* **2013**, *257*, 2607−2622.
(38) Li, Y.; Wei, X.; Han, S.; Chen, L.; Shi, J. MnO_2 Electrocatalysts Coordinating Alcohol Oxidation for Ultra-Durable Hydrogen and Chemical Productions in Acidic Solutions. *Angew. Chem., Int. Ed.* **2021**, *60*, 21464−21472.
(39) Shi, B.; Di, Z.; Guo, X.; Wei, Y.; Zhang, R.; Jia, J. Facet control of manganese oxides with diverse redox abilities and acidities for catalytically removing hazardous 1,2-dichloroethane. *Mater. Adv.* **2022**, *3*, 1101−1114.
(40) Liu, Q.; Hu, Z.; Li, L.; Li, W.; Zou, C.; Jin, H.; Wang, S.; Chou, S.-L. Facile Synthesis of Birnessite δ-MnO_2 and Carbon Nanotube Composites as Effective Catalysts for Li-CO_2 Batteries. *ACS Appl. Mater. Interfaces* **2021**, *13*, 16585−16593.
(41) Wu, Y.; Fee, J.; Tobin, Z.; Shirazi-Amin, A.; Kerns, P.; Dissanayake, S.; Mirich, A.; Suib, S. L. Amorphous Manganese Oxides: An Approach for Reversible Aqueous Zinc-Ion Batteries. *ACS Appl. Energy Mater.* **2020**, *3*, 1627−1633.
(42) Wang, D.; Wang, L.; Liang, G.; Li, H.; Liu, Z.; Tang, Z.; Liang, J.; Zhi, C. A Superior δ-MnO_2 Cathode and a Self-Healing Zn-δ-MnO_2 Battery. *ACS Nano* **2019**, *13*, 10643−10652.
(43) Chen, W.; Li, G.; Pei, A.; Li, Y.; Liao, L.; Wang, H.; Wan, J.; Liang, Z.; Chen, G.; Zhang, H.; Wang, J.; Cui, Y. A manganese−hydrogen battery with potential for grid-scale energy storage. *Nat. Energy* **2018**, *3*, 428−435.
(44) Gorlin, Y.; Jaramillo, T. F. A Bifunctional Nonprecious Metal Catalyst for Oxygen Reduction and Water Oxidation. *J. Am. Chem. Soc.* **2010**, *132*, 13612−13614.
(45) Plate, P.; Höhn, C.; Bloeck, U.; Bogdanoff, P.; Fiechter, S.; Abdi, F. F.; van de Krol, R.; Bronneberg, A. C. On the Origin of the OER Activity of Ultrathin Manganese Oxide Films. *ACS Appl. Mater. Interfaces* **2021**, *13*, 2428−2436.
(46) Chen, D.; Ding, D.; Li, X.; Waller, G. H.; Xiong, X.; El-Sayed, M. A.; Liu, M. Probing the Charge Storage Mechanism of a Pseudocapacitive MnO_2 Electrode Using in Operando Raman Spectroscopy. *Chem. Mater.* **2015**, *27*, 6608−6619.
(47) Julien, C.; Massot, M.; Baddour-Hadjean, R.; Franger, S.; Bach, S.; Pereira-Ramos, J. P. Raman spectra of birnessite manganese dioxides. *Solid State Ionics* **2003**, *159*, 345−356.
(48) Soldatova, A. V.; Balakrishnan, G.; Oyerinde, O. F.; Romano, C. A.; Tebo, B. M.; Spiro, T. G. Biogenic and Synthetic MnO_2 Nanoparticles: Size and Growth Probed with Absorption and Raman Spectroscopies and Dynamic Light Scattering. *Environ. Sci. Technol.* **2019**, *53*, 4185−4197.
(49) Morgan Chan, Z.; Kitchaev, D. A.; Nelson Weker, J.; Schnedermann, C.; Lim, K.; Ceder, G.; Tumas, W.; Toney, M. F.; Nocera, D. G. Electrochemical trapping of metastable Mn^{3+} ions for activation of MnO_2 oxygen evolution catalysts. *Proc. Natl. Acad. Sci. U.S.A.* **2018**, *115*, E5261−E5268.
(50) Zhu, G.; Zhu, W.; Lou, Y.; Ma, J.; Yao, W.; Zong, R.; Zhu, Y. Encapsulate α-MnO_2 nanofiber within graphene layer to tune surface electronic structure for efficient ozone decomposition. *Nat. Commun.* **2021**, *12*, 4152.
(51) Tran, G.-S.; Vo, T.-G.; Chiang, C.-Y. Operando Revealing the Crystal Phase Transformation and Electrocatalytic Activity Correlation of MnO_2 toward Glycerol Electrooxidation. *ACS Appl. Mater. Interfaces* **2023**, *15*, 22662−22671.
(52) Kang, H.; He, D.; Yan, X.; Dao, B.; Williams, N. B.; Elliott, G. I.; Streater, D.; Nyakuchena, J.; Huang, J.; Pan, X.; Xiao, X.; Gu, J. Cu Promoted the Dynamic Evolution of Ni-Based Catalysts for Polyethylene Terephthalate Plastic Upcycling. *ACS Catal.* **2024**, *14*, 5314−5325.
(53) Agaev, A. N.; Velieva, S. M.; Zeinalova, N. N.; Kulaliev, I. D. Hydroxyalkylbenzylsulfonates as multipurpose oil additives. *Russ. J. Appl. Chem.* **2009**, *82*, 2075−2078.
(54) Swain, C. G.; Powell, A. L.; Sheppard, W. A.; Morgan, C. R. Mechanism of the Cannizzaro reaction. *J. Am. Chem. Soc.* **1979**, *101*, 3576−3583.
(55) Basavaiah, D.; Sharada, D. S.; Veerendhar, A. Organo-base mediated Cannizzaro reaction. *Tetrahedron Lett.* **2006**, *47*, 5771−5774.
(56) Birdja, Y. Y.; Koper, M. T. M. The Importance of Cannizzaro-Type Reactions during Electrocatalytic Reduction of Carbon Dioxide. *J. Am. Chem. Soc.* **2017**, *139*, 2030−2034.
(57) Chernyshova, I. V.; Somasundaran, P.; Ponnurangam, S. On the origin of the elusive first intermediate of CO_2 electroreduction. *Proc. Natl. Acad. Sci. U.S.A.* **2018**, *115*, E9261−E9270.
(58) Gong, X.; Tong, F.; Ma, F.; Zhang, Y.; Zhou, P.; Wang, Z.; Liu, Y.; Wang, P.; Cheng, H.; Dai, Y.; Zheng, Z.; Huang, B. Photoreforming of plastic waste poly (ethylene terephthalate) via in-situ derived CN-CNTs-NiMo hybrids. *Appl. Catal., B* **2022**, *307*, 121143.

https://doi.org/10.1021/jacs.4c05512
J. Am. Chem. Soc. 2024, 146, 18639−18649